Nanoscale

Dynamic Article Links ►

Cite this: DOI: 10.1039/c0xx00000x

www.rsc.org/xxxxxx

COMMUNICATION

2D single- or double-layered vanadium oxide nanosheets assembled 3D microflowers: controlled synthesis, growth mechanism, and applications

Hongchang Pang,[a] Yongqiang Dong,[a] Siong Luong Ting,[a] Jinlin Lu,[a] Chang Ming Li,[b] Dong-Hwan Kim,[a] Peng Chen*[a]

Received (in XXX, XXX) Xth XXXXXXXXX 20XX, Accepted Xth XXXXXXXXX 20XX
DOI: 10.1039/b000000x

A facile one-pot solvent-thermal method was developed to synthesize a unique 3D microflower structure assembled from single- or double-layered 2D nanosheets of V_4O_9 (F-VO). Simply by controlling the precursor concentration, yolk-shelled V_4O_9 (YS-VO) or bulk V_4O_9 (B-VO) can be produced instead. The precursor-concentration dependent growth mechanism is proposed. The exceptional catalytic / electrochemical properties and large specific surface area of F-VO promise a wide range of applications. As the proof-of-concept demonstrations, we demonstrate its uses for high-performance supercapacitor (~392 F g^{-1}), and sensitive detection of H_2O_2 (with a low detection limit of ~0.1 μM) and methanol (with a low detection limit of ~60 μM). Furthermore, we show that F-VO greatly outperforms its counterparts (YS-VO and B-VO) presumably owing to its unique structure and crystal plane orientation.

Introduction

Due to their extraordinary structural, electrical, and physicochemical properties that are distinct to their bulk counterparts, the emerging two-dimensional (2D) ultrathin nanosheets (graphene,[1,2] metals,[3,4] metal oxides,[5,6] and transition metal chalcogenides,[7] etc.) have received tremendous interest for their applications in catalysis,[4,8-10] electronics,[7,11-13] energy devices,[14,15] and sensors.[16,17] However, synthesis of these nanosheets (particularly non-carbon materials) in scalable solution processes is highly challenging, partly, because of their high surface energy, tendency to stack and aggregate, and directional growth due to anisotropic lattice structure.[1,18]

Vanadium oxides are a family of interesting materials with exceptional catalytic, electrical and photoelectronic, and magnetic properties.[19-22] Several nanostructured vanadium oxides (such as nanowires and hollow microspheres) have been demonstrated.[23-26] Recently, ultrathin 2D nanosheets of V_2O_5 have been synthesized and employed as gas sensor and supercapacitor.[27] However, the synthetic route is complex, multi-stepped and time-consuming. Comparing to other vanadium oxides, V_4O_9 is relatively less studied. In this contribution, we report a facile one-pot solvent-thermal synthesis of a 3D microflower structure assembled from single- or double-layered 2D nanosheets of V_4O_9 (F-VO). Yolk-shell and bulk V_4O_9 can be produced by the same synthetic route simply by increasing the precursor concentration. Taking the advantages of its large specific surface area, high electrochemical activity, and excellent catalytic properties, we further demonstrate the uses of F-VO for high-performance supercapacitor and highly sensitive sensors based on different chemistry, highlighting the versatile potentials of nanostructured V_4O_9.

Experimental

Synthesis of nanostructured vanadium oxides

Nanostructured vanadium oxide (V_4O_9) was synthesized by a one-pot solvent-thermal method using vanadium oxytriisopropoxide (VIP, purchased from Sigma-Aldrich) as vanadium source. VIP was dissolved in 20 mL 2-propanol to the desired concentrations with vigorous stirring for half an hour at room temperature. Subsequently, deionized water (4:1 molar ratio to VIP) was carefully added with continuous stirring for another 20 min. The mixture was then transferred into a Teflon-lined stainless steel autoclave (50 mL capacity), sealed and heated at 180 °C for 20 h. The precipitated powders were filtered out, washed thoroughly with absolute ethanol, and dried at 60 °C for 24 h in a vacuum oven.

Characterization

The morphology of the samples was examined by field-emission scanning electron microscope (FESEM, JSM-6700F) and transmission electron microscope (TEM, Tecnai G^2 20). The XRD patterns were obtained using Rigaku D/max 2400 X-ray

diffractometer equipped with graphite monochromatized Cu Kα radiation (λ = 1.5406 Å; scan rate = 0.02 °·s^{-1}). The thickness of V_4O_9 nanosheets was revealed by an atomic force microscope (AFM, Nanoscope IIIa). The specific surface area was determined by N_2 adsorption-desorption isotherm with a Micromeritics ASAP 2010 system.

Electrochemical Measurements

Using a CHI-660D electrochemical workstation (Chenhua), the electrochemical measurements were carried out in a two-electrode Swagelok-type cell with 1.5 M KOH as the electrolyte solution. The electrodes were made by doctor-blading deposition of a mixture containing the active material (FVO, YS-VO, or B-VO), conducting carbon black (Super-P-Li), and an organic binder (poly(vinylidene difluoride)) in a weight ratio of 85:10:5 onto nickel foam.

H_2O_2 detection

F-VO or YS-VO or B-VO with defined mass was dispersed into 100 µL DMSO containing 1.46 mM 3,3',5,5'-Tetramethylbenzidine (TMB) on a shaker. After 10 minutes, the reaction was stopped by adding 100 µL of 2M sulfuric acid. After removing the precipitates by centrifugation (4000 rpm for 3 min), the absorbance of the solution was measured using a UV-vis spectrophotometer (UV 2450).

Results and discussion

The vanadium oxide nanostructures were synthesized by one-pot solvent-thermal method using vanadium oxytriisopropoxide (VIP) as the precursor and *2*-propanol as the solvent. X-ray diffraction (XRD) was used to identify the crystal composition of the as-prepared materials. The obtained XRD pattern (Fig. 1A) indicates that all of the Bragg peaks can be unambiguously indexed to an orthorhombic V_4O_9 phase (JCPDS No. 71-2248). The X-ray photoelectron spectroscopy (XPS) shows three distinct peaks corresponding to vanadium, carbon (reference) and oxygen, respectively. The peaks at 516.59 eV and 523.93 eV correspond exactly to the binding energies of V2p3/2 and 2p1/2, respectively.[30, 31] The V2p3/2 peak can be de-convoluted into two major peaks at 516.12 eV and 517.30 eV which are in exact accordance with the binding energies of V^{4+} and V^{5+}, respectively (Fig. 1B).[32] Taken together, V_4O_9 containing both V^{4+} and V^{5+} is obtained from the synthesis.

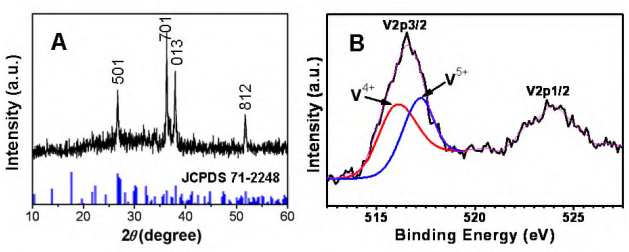

Fig. 1 (A) The XRD pattern of F-VO. The pattern shown at the bottom is the standard XRD card of V_4O_9. (B) The V2p region of the XPS spectrum of F-VO which is fitted by the addition (pink) of two Gaussian peaks at 516.12 eV (red) and 517.30 eV (blue).

As shown by field emission scanning electron microscopy (FESEM), abundant uniformly-sized V_4O_9 microflowers (F-VO, diameter ~1 µm) are obtained after one-pot solvent-thermal reaction (Fig. 2A). The petals of the microflowers are nearly transparent under a 5 kV electron beam from FESEM, suggesting their ultrathin thickness (Fig. 2B). Transmission electron microscopy (TEM) further confirms that the ultrathin petals (~0.5 µm in size) burst forth individually (Fig. 2C and D). High resolution TEM (HRTEM) shown in Fig. 2E displays the lattice fringes of one petal with regular spacing of 0.242 nm, corresponding to the (412) plane of V_4O_9. As revealed by atomic force microscopy (AFM) (Fig. 2F and G), the thickness of a single V_4O_9 nanosheet exhibits two quantized levels. The quantal step (~1 nm) is comparable to the c lattice parameter of V_4O_9 (9.396 Å, as illustrated in Fig. 2H). Evidently, V_4O_9 nanosheets are resulted from a-b in-plane growth with mono- and double-layer domains.

To understand the growth mechanism of F-VO, the SEM snapshots are taken at different time points (Fig. S1 in ESI†). As observed, non-uniform flowers are produced with 2h reaction and they reach full bloom after 20h. And interestingly, raising the precursor (VIP) concentration leads to the evolution from microflowers to yolk-shell microspheres (Fig. 3). The VIP concentration dependent growth mechanism is illustrated in Fig.4.

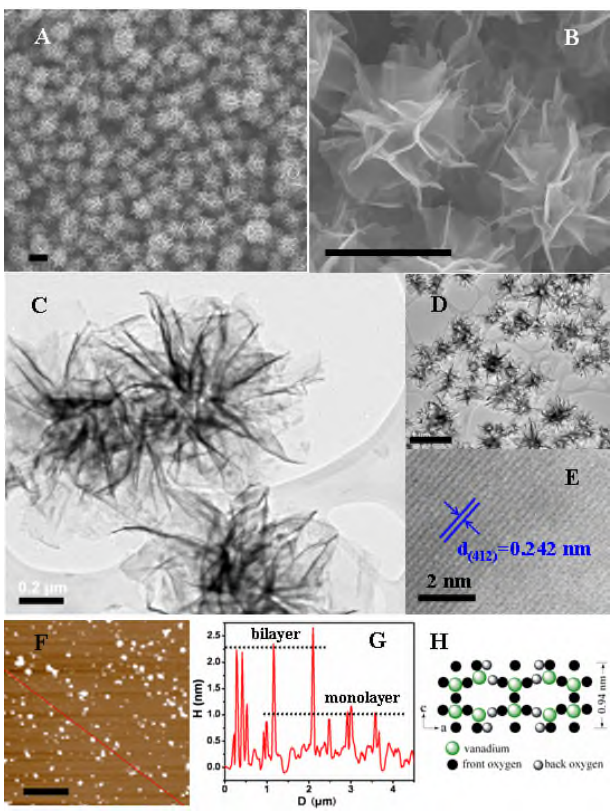

Fig. 2 (A and B) SEM images of F-VO. (C and D) TEM images of F-VO. (E) High resolution TEM of F-VO. The scale bars in (A), (B), (D) and (F) are 1 µm. (F) AFM image of V_4O_9 nanosheets from F-VO. (G) AFM height profile along the line shown in (F). (H) The schematic crystal structure of V_4O_9 viewed along the *b*-axis of the orthorhombic structure.

As discussed in our previous report,[28] the yolk-shell (YS-VO) structure is formed *via* two-step self-assembly of hydrolysate nanoparticles (NP) (21.19 mM VIP), during which the initially formed hydrophilic NP-yolk is solved by a H_2O layer and a thin shell subsequently forms at the interface between the H_2O solvation layer and the surrounding hydrophobic *2*-propanol. When VIP concentration is low (10.6 mM VIP), conceivably, the large aggregation (yolk) cannot form; instead small nuclei result. In addition, at a low VIP concentration, the crystal growth is slow and prone to be oriented leading to the formation of 2D sheet. The cluster of 2D sheets in F-VO may be originated from simultaneous growth from a few aggregated nuclei. At a very high VIP concentration (over 100 mM), bulk V_4O_9 (B-VO) is yielded probably due to drastic aggregation of nuclei and fast growth rate in all directions.

We demonstrate that differently structured V_4O_9 materials are obtained simply by varying the precursor concentration. Among them, the microflower structure (3D assembly of 2D nanosheets) should have the largest surface area. Indeed, as determined by N_2 adsorption-desorption isotherm, the specific surface area of F-VO is ~107.9 m^2 g^{-1} which is much larger than that of yolk-shell microspheres (~58.7 m^2 g^{-1}) and bulk V_4O_9 (16.3 m^2 g^{-1}) (Fig. 5). Large active area should lead to superior electrochemical activities of F-VO.

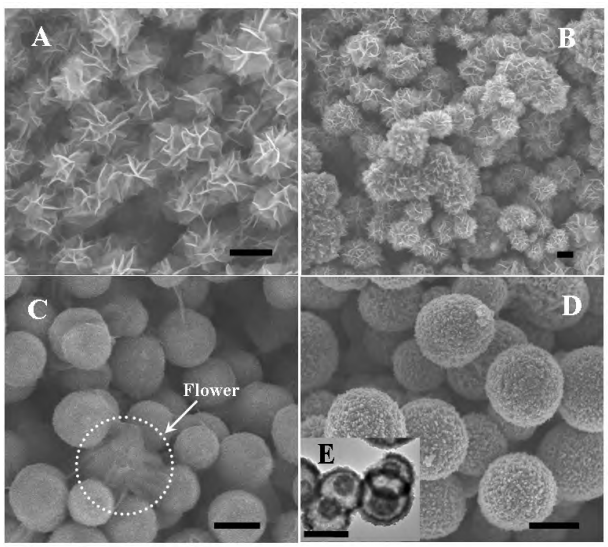

Fig. 3 SEM images of V_4O_9 structures synthesized with VIP concentration of 10.6 mM (A), 12.71 mM (B), 19.07 mM (C) and 21.19 mM (D). The inset in (D) is the TEM image to reveal the yolk-shell structure. All scale bars are 1 μm.

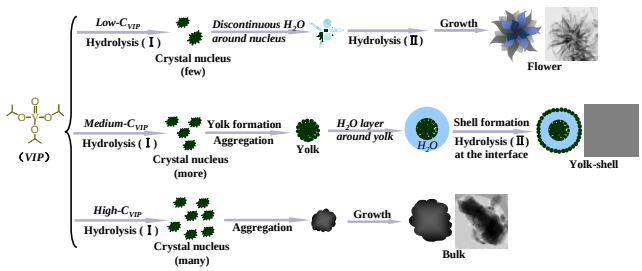

Fig. 4 Schematic illustration of the growth mechanisms of three different V_4O_9 structures synthesized at different concentrations of VIP.

As a proof-of-concept demonstration, we investigated the application of F-VO for supercapacitors. Vanadium exhibits oxidation states of +2, +3, +4 and +5; and V_4O_9 is a mixed-valence compound containing both V^{4+} and V^{5+}. We hypothesize that V_4O_9 would offer large pseudo-capacitance resulting from transition between the different oxidation states and its large specific surface area. In a symmetric two-electrode configuration, the cyclic voltammograms (CVs) at various scan rate were measured from the V_4O_9 electrodes in 1.5 M KOH electrolyte (Fig. 6A). The near-rectangular CV curves indicate the high capacitance of the F-VO electrode. From the charge-discharge voltage profile (Fig. 6B), the specific capacitance (*Cs*) is calculated according to the equation $Cs = 4 \times (I \times \Delta t)/(m \times \Delta V)$, where I is the constant discharge current, Δt is the discharge time, m is the total mass of F-VO on both electrodes, ΔV is the voltage difference between the voltage after ohmic drop at the beginning of discharging and the voltage at the end of discharging.[33] The specific capacitance of F-VO electrode is found to be as high as 392 F g^{-1} at the current density of 0.5 A g^{-1}. As shown in Fig. 6C,

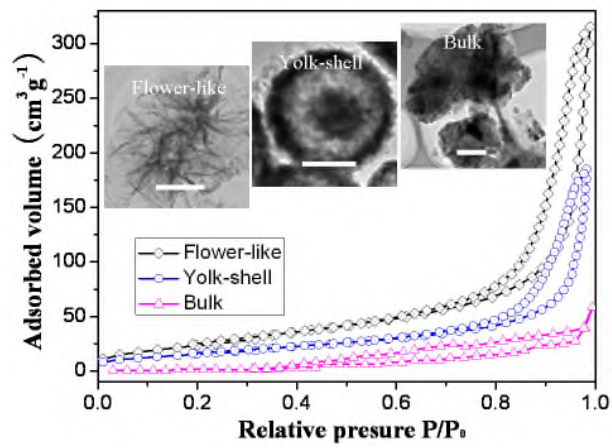

Fig. 5 N_2 adsorption-desorption isotherm for different V_4O_9 structures. All scale bars in the insets are 500 nm.

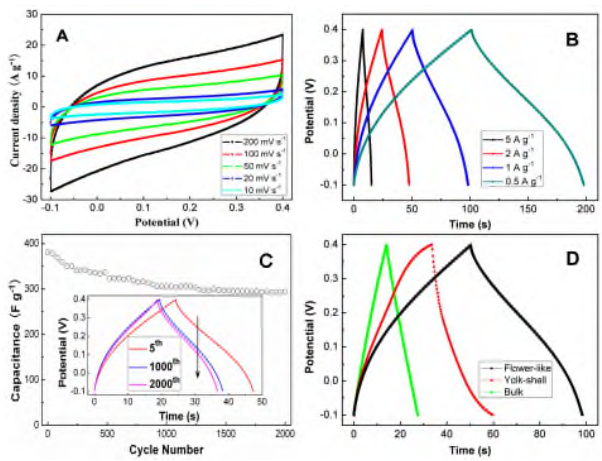

Fig. 6 (A) CVs of F-VO at various scan rates. (B) Charge-discharge curves of F-VO at different current densities. (C) The cycling stability of the specific capacitance of F-VO at 2 A g^{-1}. The inset shows the charge-discharge curves at different cycle numbers. (D) Comparison of charge-discharge curves from F-VO, YS-VO and B-VO at 1 A g^{-1}.

75% of the capacitance is retained even after 2000 cycles. Such high stability might be ascribed to that the unique flower-like structure assembled from ultrathin and well-seperated nanosheets is less prone to structural alteration caused by repetitive redox reactions during charge-discharge cycles. In comparison, the specific capacitance of yolk-shell vanadium oxide (~238 F g^{-1}) and bulk vanadium oxide (~83 F g^{-1}) are much smaller at the same current density (Fig. 6D).

Like other transition metal compounds, vanadium compounds can act as good catalysts because of their ability to readily transit between their oxidation states.[34, 35] As an example, we here examined the catalytic ability of F-VO towards hydrogen peroxide (H_2O_2) which is an important biological signaling molecule, by-product of many biological processes, and environmental hazard at high concentrations. Conventionally, H_2O_2 detection relies on naturally occurring peroxidases, most notably, horseradish peroxidase (HRP). But these proteins are not only costly but also of poor tolerance to non-physiological conditions. We expect high peroxidase-like activity of flower-like V_4O_9 (F-VO) because of its ability to act as a strong electron donor (*via* converting V^{4+} to V^{5+} intermediate) and full exposure of vanadium atoms in the monolayer structure.

Using 3,3',5,5',-tetramethylbenzidine (TMB) as the redox mediator and color reporter of peroxidase activity,[36, 37] we compared the catalytic activity of F-VO and HRP in the presence of 2.21 mM H_2O_2 using UV-Vis absorbance spectroscopy. As shown in Fig. 7A, 50 µg F-VO exhibits similar catalytic activity as 2.5 µg of HRP, suggesting the F-VO as a low-cost and robust alternative to peroxidases. In line with our observation, the peroxidase property of vanadium pentoxide (V_2O_5) nanowires has recently been demonstrated.[38] The dose response curve (absorption *vs.* H_2O_2 concentration) shown in Fig. 7B demonstrates that 0.1 µM H_2O_2 can be unambiguously resolved (with signal-to-noise ratio of 15). Such outstanding sensitivity of the F-VO based optical detection outperforms the recently developed electrochemical sensors based on HRP functionalized graphene electrodes.[39, 40] In comparison to F-VO, the sensitivity of YS-VO and B-VO is one order lower (Fig. 7B). In addition to the larger specific surface area, the higher catalytic activity of F-VO may be attributable to its unique crystal planes. Indeed, the XRD pattern of F-VO are distinct to that of YS-VO and B-VO (comparing Fig. 1A with Fig. S2 in ESI).

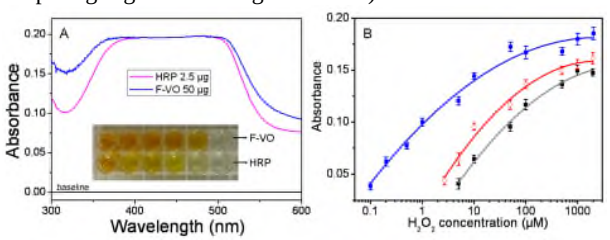

Fig. 7 (A) UV-Vis absorbance of DMSO solution containing 1.46 mM TMB and 2.21 mM H_2O_2, in the presence of 50 µg F-VO or 2.5 µg HRP. The inset shows the photograph of the test solutions containing various amounts of F-VO (from right to left in the top row: 0, 50, 75, 100, 125, 150 µg) or various amounts of HRP (from right to left in the bottom row: 0, 0.5, 1, 1.5, 2, 2.5 µg). (B) UV-Vis absorbance curve (with polynomial fitting) of 75 µg F-VO (blue) or YS-VO (red) or B-VO (black) at varying H_2O_2 concentrations. The error bars indicate the standard deviations from 4 independent measurements.

Because the oxidative ability of V^{5+} (*via* its conversion to V^{4+}), V_4O_9 shall be able to act as oxidation catalyst for many substances. Here, we show that F-VO coated glassy carbon electrode can electrochemically detect methanol with a low detection limit of ~60 µM which is much lower than that of YS-VO and B-VO based electrodes (Fig. S3 and S4 in ESI). The detection is based on oxidation of methanol catalyzed by reduction of V^{5+} to V^{4+}. Furthermore, the electrode can be recovered and re-used by bubbling oxygen into the solution.

Conclusions

In summary, a simple one-pot solvent-thermal synthetic route is devised to produce a unique flower-like microstructure assembled from ultrathin sheets of vanadium oxide. The precursor-concentration dependent growth mechanism is discussed. We further demonstrate the use of such uniquely structured transition metal oxide as high-performance supercapacitor and highly efficient catalysts for sensing applications. To the best of our knowledge, the herein demonstrated V_4O_9 monolayer sheet is a new addition to the growing family of 2D nanosheets. This study highlights the versatile and exceptional potentials of this fascinating material arisen from the interesting chemistry of valence transition of vanadium and large active surface area of such 2D crystal.

Acknowledgement

This work is financially supported by the Agency for Science, Technology and Research (A*STAR) under SERC Grant No. 102 170 0142.

Notes and references

[a] *School of Chemical and Biomedical Engineering, Nanyang Technological University, 70 Nanyang Drive, 637457, Singapore, E-mail: chenpeng@ntu.edu.sg*
[b] Institute for Clean Energy & Advanced Materials, Southwest University, Chongqing ,400715, P.R. China

† Electronic Supplementary Information (ESI) available: Evolution SEM images of F-VO over reaction time, XRD patterns of as-prepared YS-VO and B-VO, amperometric response and cyclic voltammetry (CV) measurements of the as-prepared differently nanostructured vanadium oxides for methanol detection information. See DOI: 10.1039/b000000x/

1 Zhu, Y. W.; Murali, S.; Cai, W. W.; Li, X. S.; Suk, J. W.; Potts, J. R.; Ruoff, R. S. *Adv. Mater.* **2010**, *22*, 3906-3924.
2 Li, D.; Müller, M. B.; Gilje, S.; Kaner, R. B.; Wallace, G. G. *Nature Nanotech.* **2008**, *3*, 101-105.
3 Siril, P. F.; Ramos, L.; Beaunier, P.; Archirel, P.; Etcheberry, A.; Remita, H. *Chem. Mater.* **2009**, *21*, 5170-5175.
4 Huang, X.; Tang, S.; Mu, X.; Dai, Y.; Chen, G.; Zhou, Z.; Ruan, F.; Yang, Z.; Zheng, N. *Nature Nanotech.* **2011**, *6*, 28-32.
5 Choi, M.; Na, K.; Kim, J.; Sakamoto, Y.; Terasaki, O.; Ryoo, R. *Nature*, **2009**, *461*, 246-249.
6 Yu, T.; Lim, B.; Xia. Y. *Angew. Chem. Int. Ed.* **2010**, *49*, 4484-4487.
7 Wang, Q. H.; Kalantar-Zadeh, K.; Kis, A.; Coleman, J. N.; Strano, M. S. *Nature Nanotech.* **2012**, *7*, 699-712.
8 Liu, K. K.; Zhang, W.; Lee, Y. H.; Lin, Y. C.; Chang, M. T.; Su, C. Y.; Chang, C. S.; Li, H.; Shi, Y.; Zhang, H.; Lai, C. S.; Li, L. J. *Nano Lett.* **2012**, *12*, 1538-1544.
9 Chen, D.; Feng, H.; Li, J. H. *Chem. Rev.* **2012**, *112*, 6027-6053.
10 Liang, Y.; Li, Y.; Wang, H.; Zhou, J.; Wang, J.; Regier, T.; Dai, H. *Nature Mater.* **2011**, *10*, 780-786.

11 Dreyer, D. R.; Jia, H. P.; Bielawski, C. W. Graphene Oxide: *Angew. Chem. Int. Ed*. **2010**, *122*, 6965-6968.
12 Xia, F.; Farmer, D. B.; Lin, Y.; Avouris, P. *Nano Lett*. **2010**, *10*, 715–718.
13 Chen, F.; Qing, Q.; Xia, J.; Li, J.; Tao, N. *J. Am. Chem. Soc*. **2009**, *131*, 9908-9909.
14 Wu, J.; Pisula, W.; Müllen, K. *Chem. Rev*. **2007**, *107*, 718-747.
15 Dong, X.; Xu, H.; Wang, X.; Huang, Y.; Chan-Park, M. B.; Zhang, H.; Wang, L. H.; Huang, W.; Chen, P. *ACS Nano*. **2012**, *6*, 3206-3213.
16 Yong, Y. C.; Dong, X.; Chan-Park, M. B.; Song, H.; Chen, P. *ACS Nano*. **2012**, *6*, 2394-2400.
17 Chen, S.; Xing, W.; Duan,J.; Hu, X.; Qiao, S. Z. J Mater. Chem. A. **2013**, 1, 2941-2954.
18 Li, W.; Geng, X.; Guo, Y.; Rong, J.; Gong, Y.; Wu, L.; Zhang, X.; Li, P.; Xu, J.; Cheng, G.; Sun, M.; Liu, L. *ACS Nano*, **2011**, *5*, 6955-6961.
19 Liu, Y.; Dong, X.; Chen, P. *Chem. Soc. Rev*. **2012**, *41*, 2283-2307.
20 Butler, S. Z.; Hollen, S. M.; Cao, L.; Cui, Y.; Gupta, J. A.; Gutiérrez, H. R.; Heinz, T. F.; Hong, S. S.; Huang, J.; Ismach, A. F.; Johnston-Halperin, E.; Kuno, M.; Plashnitsa, V. V.; Robinson, R. D.; Ruoff, R. S.; Salahuddin, S.; Shan, J.; Shi, L.; Spencer, M. G.; Terrones, M.; Windl, W.; Goldberger, J. E. *ACS Nano*, **2013**, 7, 2898-2826.
21 Mai, L.; Xu, L.; Han, C.; Xu, X.; Luo, Y.; Zhao, S.; Zhao, Y. *Nano Lett*. **2010**, *10*, 4750–4755.
22 Wang, Y.; Cao, G. Z. *Adv. Mater*. **2008**, *20*, 2251-2269.
23 Liu, J.; Wang, X.; Peng, Q.; Li, Y. *Adv. Mater*. **2004**, *17*, 764-767.
24 Sathiya, M.; Prakash, A. S.; Ramesha, K.; Tarascon, J. M.; Shukla, A. K. *J. Am. Chem. Soc*. **2011**, *133*, 16291-16299.
25 Xiong, C.; Aliev, A.; Gnade, B.; Balkus, K. J. *ACS Nano*, **2008**, *2*, 293-301.
26 Tremel, W.; Natalio, F.; Andre, R.; Hartog, A. F.; Stoll, B.; Jochum, K. P.; Wever, R. *Nature Nanotech*. **2012**, *7*, 530-535.
27 Cao, A. M.; Hu, J. S.; Liang, H. P.; Wan, L. J. *Angew. Chem. Int. Ed*. **2005**, *44*, 4391-4395.
28 Pang, H.; Chen, P.; Yang, H.; Lu, J.; Guo, C. X.; Ning, G.; L. C. M. *Chem. Commun*. **2013**, *49*, 1536-1538.
29 Rui, X.; Lu, Y.; Yin, Z.; Sim, D. H.; Xiao, N.; Lim, T. M.; Hng, H. H.; Zhang, H.; Yan, Q. *Small*, **2012**, *9*, 716-721.
30 Zhou, X.; Wu, G.; Gao, G.; Cui, C.; Yang, H.; Shen, J.; Zhou, B.; Zhang, Z. *Electrochim. Acta*. **2012**, *74*, 32-38.
31 Jiao, L.; Yuan, H.; Wang, Y.; Cao, J.; Wang, Y. *Electrochem. Commun*. **2005**, *7*, 431-436.
32 Overmeere, Q. V.; Kerman, K.; Ramanathan, S. *Nano Lett*. **2012**, *12*, 3756-3760.
33 Zhang, L.; Zhao, X. S. *Chem. Soc. Rev*. 2009, *38*, 2520-2531.
34 Veitch, N. C.; Smith, A. T. *Academic, New York*, **2001**, *51*, 107-162.
35 Berglund, G. I.; Carlsson, G. H.; Smith, A. T.; Szoke, H.; Henriksen, A.; Hajdu J. *Nature*, **2002**, *417*, 463-468.
36 Szili, E. J.; Jane, A.; Low, S. P.; Sweetman, M.; Macardle, P.; Kumar, S.; Smart, R. S. C.; Voelcker, N. H. *Sensors and Actuators B*, **2011**, *160*, 341-348.
37 Rodriguez-Lopez, J. N.; Lowe, D. J.; Hernandez-Ruiz, J.; Hiner, A. N. P.; Garcia-Canovas, F.; Thorneley, R. N. F. *J. Am. Chem. Soc*. **2001**, *123*, 11838-11847.
38 Natalio, F.; Andre, R.; Hartog, A. F.; Stoll, B.; Jochum, K. P.; Wever, R.; Tremel, W. *Adv. Funct. Mater*. **2011**, *21*, 501-509.
39 Dong, X.; Ma, Y.; Zhu, G.; Huang, Y.; Wang, J.; Chan-Park, M. B.; Wang, L.; Huang, W.; Chen, P. *Journal of Materials Chemistry*, **2012**, *22*, 17044-17048.
40 Guo,Y.; Deng, L.; Li, J.; Guo, S.; Wang, E.; Dong, S. *ACS Nano*. **2011**, *5*, 1282-1290.